EFFICIENT ANALYSIS OF HALE AIRCRAFT STRUCTURE FOR STATIC AND DYNAMIC AEROELASTIC BEHAVIOR

Lu LIU[1], Taehyoun KIM[2], Kwok Leung LAI[3]

[1]Department of Mechanical Engineering, National University of Singapore
Faculty of Engineering, NUS, 3 Engineering Drive 2, Blk E1 #05-15 Singapore 117578
liulu02@u.nus.edu

[2]Department of Mechanical Engineering, National University of Singapore
Faculty of Engineering, NUS, 9 Engineering Drive 1, Blk EA, #07-15, Singapore 117576
mpekimt@nus.edu.sg

[3] Temasek Laboratories, National University of Singapore, Singapore
Temasek Laboratories, NUS, 5A,Engineering Drive 1, #09-02, Singapore 117411
tsllaikl@nus.edu.sg

Keywords: large deformation, HALE, static, UVLM

Abstract: In this work, the static aeroelastic behavior of high aspect ratio wings undergoing large static deformations has been investigated analytically. Towards this end, a nonlinear structural model based on a simple one-dimensional nonlinear beam theory originally developed by Minguet and Dugundji [1] is used. An efficient evaluation of large static deformation of High Altitude Long Endurance (HALE) airplane is developed by merging the wing, fuselage, and tail structures based on the beam model. This paper also discusses coupling the beam model with several aerodynamic models to investigate the static performance of the high aspect ratio wing. Comparisons of the aerodynamic tools are made in terms of numerical efficiency, simplicity and further applications. Among these aerodynamic modeling, unsteady vortex lattice method (UVLM) is given a special attention since it offers convenient and accurate prospects in analyzing the dynamic behavior of the HALE aircraft.

1 INTRODUCTION

The prediction of the dynamic and aeroelastic behavior of the high aspect ratio wing under various flight conditions is a major task in designing the high altitude long endurance (HALE) airplane. In particular, an accurate and efficient structural model of the high aspect ratio wing that is capable of handling nonlinear large deflections is necessary. The aeroelastic behavior of HALE airplane can be analyzed by combining the nonlinear structural model with general aerodynamic theories.

The structural model used in this paper to deal with deflections and rotations of the flexible wing without any limitation on the magnitudes originates from a previous work by Minguet and Dugundji [1]. In this formulation, Euler angles are utilized to account for the large deformation, and does not rely on any approximate expansion of these angles. No ordering scheme is introduced and all geometric nonlinearities are retained fully [2]. A total of twelve nonlinear partial differential equations that represent compatibility and equilibrium constitute a two-point boundary value problem with proper boundary conditions at the root and tip of the beam. The stress-strain relation in its most general form that includes various couplings

due to the use of composite materials are presented. The static solutions of these differential equations can be obtained by a numerical integration scheme such as Runge-Kutta algorithm combined with a Newton-Raphson type iteration [3].

Based on the aforementioned work, a new model capable of free vibrational and aeroelastic analysis for a high aspect ratio wing-fuselage-tail combination has been developed and is introduced in this paper. Every substructure of the airplane, i.e., wing, fuselage, tails, is assumed to behave like a high aspect ratio beam, which is appropriate and acceptable for the HALE aircraft. The predescribed beam model is applied to each substructure respectively, while the interactions and relations at the junctions between adjacent parts are established.

Later, the structural beam model will be combined with a vortex element model based on the unsteady vortex lattice method (UVLM) for aeroelastic analysis. Currently, the use of UVLM has been gaining a ground in the study of non-stationary problems in which free-wake methods become a necessity because of geometric complexity, such as flapping wing kinematics, morphing wings, and rotorcraft among others [4]. The pioneering works in the development of UVLMs were carried out by Belotserkovskii, Rehbach, and researchers at Virginia Tech and Technion as stated by Roccia et al [4]. Katz and Plotkin [5] provide a comprehensive description of the UVLM and its applications. The present numerical model is an extension of the widely used three dimensional general unsteady vortex-lattice model [5] and provides an attractive compromise between computational cost and fidelity.

2 STATIC LARGE DEFLECTION BEAM MODEL

2.1 Assumptions

To completely represent the nonlinearities due to arbitrarily large deflections and rotations, a set of twelve first-order, nonlinear differential equations developed by Minguet and Dugundji [1] is used in the present analysis. Before presenting all the necessary equations for the large nonlinear static deflection modeling, one the basic assumptions of the classical beam theory will be briefly reviewed. The first assumption is that the beam is much longer in one direction and its cross-section is undeformable, and hence will not change the shape under loads. This allows one to reduce the problem to one-dimensional model where all the displacements are functions of only one coordinate, namely the beam arc length s measured along some reference line. This assumption is true for HALE airplane and will therefore be retained here. Based on this assumption, the beam position in space is completely describable by the position of its reference line. As shown in Fig. 1, two coordinates systems are introduced: the global coordinates system (x,y,z) that remains fixed in space at all times and the local axes system (ξ, η, ζ) that follows the beam cross-section during its motion. For the time being, it will be assumed that the transverse shear strains in the cross-section can be neglected so that the cross-section is presumed to remain orthogonal to the reference line.

2.2 Basic Equations

The governing equations are obtained by considering equilibrium, strain-displacement compatibilities, linear stress-strain relations of a beam element, and are not based on any ordering schemes that typify most of moderate deflection equations. For thorough derivation of the equations see Minguet and Dugundji [1]. All of the equations are derived based on the following transformation matrix that transforms the global coordinates into the local ones (see

Fig. 1). To describe the deformation of the beam, the reference line position is identified by its three displacements u, v, w measured along the global axes. The attitude of the cross-section, and thus of the local axes system, is described with the use of the three Euler angles ψ, β, θ via the use of a transformation matrix T from the global to the local axes.

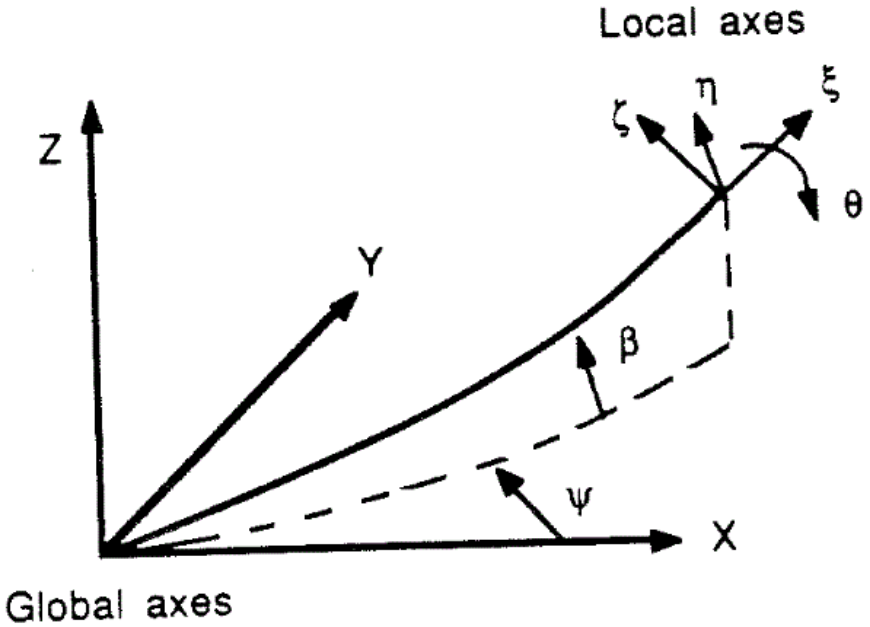

Figure 1: Illustration of Local and Global Axes and of Euler Angles

$$\begin{bmatrix} \vec{l}_\xi \\ \vec{l}_\eta \\ \vec{l}_\zeta \end{bmatrix} = [T] \begin{bmatrix} \vec{l}_x \\ \vec{l}_y \\ \vec{l}_z \end{bmatrix} \tag{1}$$

$$\begin{bmatrix} \xi \\ \eta \\ \zeta \end{bmatrix} = \begin{bmatrix} 1 & 0 & 0 \\ 0 & \cos\theta & \sin\theta \\ 0 & -\sin\theta & \cos\theta \end{bmatrix} \begin{bmatrix} \cos\beta & 0 & \sin\beta \\ 0 & 1 & 0 \\ -\sin\beta & 0 & \cos\beta \end{bmatrix} \begin{bmatrix} \cos\psi & \sin\psi & 0 \\ -\sin\psi & \cos\psi & 0 \\ 0 & 0 & 1 \end{bmatrix} \begin{bmatrix} x \\ y \\ z \end{bmatrix} \tag{2}$$

$$[T] = \begin{bmatrix} \cos\beta\cos\psi & \cos\beta\sin\psi & \sin\beta \\ -\cos\theta\sin\psi & -\cos\theta\sin\psi & \sin\theta\cos\beta \\ -\sin\theta\sin\beta\cos\psi & -\sin\theta\sin\beta\cos\psi & \\ -\cos\theta\sin\psi & -\cos\theta\sin\psi & \cos\theta\cos\beta \\ -\sin\theta\sin\beta\cos\psi & -\sin\theta\sin\beta\cos\psi & \end{bmatrix} \tag{3}$$

The transformation matrix is orthogonal and related to the rotation or curvature matrix as follows:

$$[T]^{-1} = [T]^T \tag{4}$$

$$\frac{d[T]}{ds} = [\omega][T] \tag{5}$$

with $$[\omega] = \begin{bmatrix} 0 & \omega_\zeta & -\omega_\eta \\ -\omega_\zeta & 0 & \omega_\xi \\ \omega_\eta & -\omega_\xi & 0 \end{bmatrix}$$

ω_ξ = twist rate

ω_η = bending curvature around η axis

ω_ζ = bending curvature around ζ axis

Then the following compatibility equations can be found from (5):

$$\frac{d\theta}{ds} = \omega_\xi - sin\theta \cdot tan\beta \cdot \omega_\eta - cos\theta \cdot tan\beta \cdot \omega_\zeta$$

$$\frac{d\beta}{ds} = -cos\theta \cdot \omega_\eta + sin\theta \cdot \omega_\zeta \tag{6}$$

$$\frac{d\psi}{ds} = \frac{sin\theta}{cos\beta} \cdot \omega_\eta + \frac{cos\theta}{cos\beta} \cdot \omega_\zeta$$

For this large deflection problem, the beam deformed position is taken into account while evaluating equilibrium equations for a differential element of the beam reference line. On every cross-section, the internal force and moment vector can be defined in the local coordinate:

$$\vec{F} = F_1\vec{I}_\xi + F_2\vec{I}_\eta + F_3\vec{I}_\zeta \tag{7}$$

$$\vec{M} = M_1\vec{I}_\xi + M_2\vec{I}_\eta + M_3\vec{I}_\zeta \tag{8}$$

Equilibrium equations can be derived by considering an infinitesimal element of length ds with forces $\vec{F}$ and moment $\vec{M}$ acting on one side and $\vec{F} + d\vec{F}$ and $\vec{M} + d\vec{M}$ on the other side as shown in Figure 2. Distributed loads measured in the global coordinate $\vec{P}^G, \vec{M}^G$, like gravity, and distributed loads measured in the local coordinate $\vec{P}^L, \vec{M}^L$, like aerodynamics are considered as applied on this element.

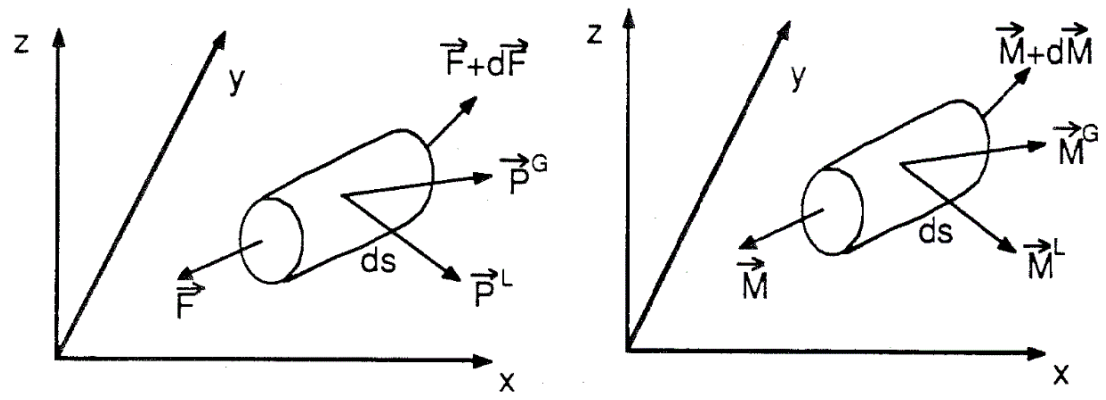

Figure 2: Illustration of Force and Moment Equilibrium

The following three nonlinear force equilibrium equations and three nonlinear moment equilibrium equations can be written:

$$\frac{dF_1}{ds} = \omega_\zeta F_2 - \omega_\eta F_3 - T_{11}P_1^G - T_{12}P_2^G - T_{13}P_3^G - P_1^L$$

$$\frac{dF_2}{ds} = -\omega_\zeta F_1 + \omega_\xi F_3 - T_{21}P_1^G - T_{22}P_2^G - T_{23}P_3^G - P_2^L \tag{9}$$

$$\frac{dF_3}{ds} = \omega_\eta F_1 - \omega_\xi F_2 - T_{31}P_1^G - T_{32}P_2^G - T_{33}P_3^G - P_3^L$$

$$\frac{dM_1}{ds} = \omega_\zeta M_2 - \omega_\eta M_3 - T_{11}M_1^G - T_{12}M_2^G - T_{13}M_3^G - M_1^L$$

$$\frac{dM_2}{ds} = -\omega_\zeta M_1 + \omega_\xi M_3 - T_{21}M_1^G - T_{22}M_2^G - T_{23}M_3^G - M_2^L + F_3 \tag{10}$$

$$\frac{dM_3}{ds} = \omega_\eta M_1 - \omega_\xi M_2 - T_{31}M_1^G - T_{32}M_2^G - T_{33}M_3^G - M_3^L + F_2$$

Next, a set of compatibility equations relating coordinates and Euler angles can be derived using the transformation matrix:

$$\begin{bmatrix} dx \\ dy \\ dz \end{bmatrix} = [T]^T \begin{bmatrix} (1+\varepsilon)ds \\ 0 \\ 0 \end{bmatrix} \tag{11}$$

$$\frac{dx}{ds} = (1+\varepsilon)\cdot\cos\theta\cdot\cos\psi$$

$$\frac{dy}{ds} = (1+\varepsilon)\cdot\cos\theta\cdot\sin\psi \tag{12}$$

$$\frac{dz}{ds} = (1+\varepsilon)\cdot\sin\beta$$

where ε is the axial strain along the reference line and x,y,z represent the global coordinates of the deformed reference line.

Finally, a set of generalized stress-strain relations are incorporated via the following six linear equations.

$$\begin{bmatrix} F_1 \\ F_2 \\ F_3 \\ M_1 \\ M_2 \\ M_3 \end{bmatrix} = \begin{bmatrix} E_{11} & E_{12} & E_{13} & E_{14} & E_{15} & E_{16} \\ & E_{22} & E_{23} & E_{24} & E_{25} & E_{26} \\ & & E_{33} & E_{34} & E_{35} & E_{36} \\ & & & E_{44} & E_{45} & E_{46} \\ & SYM & & & E_{55} & E_{56} \\ & & & & & E_6 \end{bmatrix} \cdot \begin{bmatrix} \varepsilon \\ \gamma_{\xi\eta} \\ \gamma_{\xi\zeta} \\ \omega_\xi \\ \omega_\eta \\ \omega_\zeta \end{bmatrix} \tag{13}$$

Here $\gamma_{\xi\eta}$ and $\gamma_{\xi\zeta}$ represent the two transverse shear strains. In its most general form, the above stiffness matrix can be full, i.e., there can be elastic couplings between all of the force resultants, three moment resultants and all of six strain components. The calculations of the two shear strains are ignored in the current analysis.

2.3 Boundary Conditions

The twelve differential equations and the general stress-strain relations constitute a two-point boundary value problem. For a cantilevered beam, all the forces and moments are known at the tip of the beam, and all angles and displacements are given at the root of the beam:

$$\begin{aligned} &\text{@ Tip:} \quad \left[F_1 \; F_2 \; F_3 \; M_1 \; M_2 \; M_3\right]^T = \left[0 \; 0 \; 0 \; 0 \; 0 \; 0\right]^T \\ &\text{@ Root:} \quad \left[\theta \; \beta \; \psi \; x \; y \; z\right]^T = \left[\theta_r \; \beta_r \; \psi_r \; x_r \; y_r \; z_r\right]^T \end{aligned} \tag{14}$$

2.4 Solution Procedure

All the necessary equations have now been obtained for the static large deflection modeling. Everything considered, there are twelve unknowns, i.e., three force components, three moments, three angles and three displacements, after eliminating the curvatures and strains by inverting stress-strain relations. Corresponding to these twelve unknowns, there are also twelve first-order nonlinear differential equations.

To solve the system, these equations are first discretized by dividing the beam into a finite number of elements. The twelve equations are integrated from the tip to the root of the beam using a simple and fast Runge-Kutta algorithm. In the numerical integration, one has to guess boundary values of coordinates and Euler angles at the tip and all the coordinates and Euler angles at the root need to be as close to the prescribed values as possible. Since the initial guesses are not perfect, there will be nonzero residues when the integration reaches the root. A Newton-Raphson type algorithm can then be employed to produce a better set of tip boundary values based on the current values:

$$X_r^n = f\left(X_t^n\right) \tag{15}$$

where $X_t^n = [\theta \; \beta \; \psi \; x \; y \; z]^T$ at the tip, $X_r^n = [\theta \; \beta \; \psi \; x \; y \; z]^T$ at the root.

$$X_t^{n+1} = X_t^n - J\left(X_t^n\right)^{-1} \cdot R^n \tag{16}$$

where $$R^n = f(X_t^n) - X_r$$

$$X_r = [\theta_r\ \beta_r\ \psi_r\ x_r\ y_r\ z_r]^T$$

and J is Jacobian matrix and the subscript n refers to the nth iterative values. The nth boundary values X_t^n at the tip will eventually march to the true solution.

2.5 Validation of the Beam Model for Large Static Deflections

An experimental result on a very flexible Titanium beam obtained by Pai [6] is used to verify the implementation of the beam theory. The dimensions of the beam are $479.0 \times 50.8 \times 0.45$ mm, with mass density $4430\ kg/m^3$, Young's modulus 127GPa, and Poisson's ratio 0.36. Experiments in [6] were performed with an undeformed beam in the vertical direction and clamped at one end in a horizontal position. Under the influence of gravity only, the experimental value of the static vertical deformation of the beam tip is -0.127m. The analytical value obtained using the present beam model is -0.126m, which is about 27.1% of its length. The error is less than 0.8% and the computation time on MATLAB is within one second. For this loading, only 3 iterations of Newton-Raphson procedures are needed and 3 elements are sufficient to get an accurate enough result.

3 EXTENSION TO WING-BODY-TAIL CONFIGURATION

The advantage of the beam model to consider large deformations can be extended to the whole HALE airplane if we split the airplane into regions of small and large deformations, typically, fuselage/vertical fin and wings/tail. Whether the displacements are small or large, the beam model can be directly applied to each substructure respectively.

3.1 Structural Wing-body-tail Model

For simplicity, the nose of the fuselage is assumed to be fixed. It is acceptable to assume that the fuselage, the wing, the vertical fin and the tail all behave like a high aspect ratio beam. At junctions, for one substructure the junction is considered to be root of the beam model, and a deformed shape of the other substructure will give the boundary condition of the beam at the junction. If the location of the junction is at a non-root position of the beam, the force and moment at the root of the other beam models at the junction will be regarded as applied loads to this beam at the junction. Take the junction between the fuselage and the wing as an example. The deformed shape of the fuselage at the junction, including the Euler angles and global coordinates will be the root boundary of both the left side and the right side of the wing. Since all the subsections share the same global coordinate, the coordinate of the fuselage at the junction $[x, y, z]_{fuselage}$ will be directly used as the coordinate boundary conditions at the root of the two sides of wing.

$$\left[x_r\ \ y_r\ \ z_r\right]^T_{left\text{-}wing} = \left[x_r\ \ y_r\ \ z_r\right]^T_{right\text{-}wing} = \left[x_j\ \ y_j\ \ z_j\right]^T_{fuselage} \tag{17}$$

But since each beam model uses its own local coordinates, the Euler angles of the fuselage at the junction $[\theta, \beta, \psi]_{fuselage}$ need to be modified according to the relationship between those local coordinates, which will be retained during deformation. Suppose $[T]_{fuselage-left\_wing}$ and $[T]_{fuselage-right\_wing}$ represent the transformation matrices from the local coordinate of the fuselage to that of the left wing and the right wing,

respectively. The Euler angle boundary conditions at the root of the wings can be calculated from the following equations:

$$\begin{aligned} T\left(\left[\theta_r \;\; \beta_r \;\; \psi_r\right]^T_{left-wing}\right) &= [T]_{fuselage-left\_wing}\, T\left(\left[\theta_j \;\; \beta_j \;\; \psi_j\right]^T_{fuselage}\right) \\ T\left(\left[\theta_r \;\; \beta_r \;\; \psi_r\right]^T_{right-wing}\right) &= [T]_{fuselage-right\_wing}\, T\left(\left[\theta_j \;\; \beta_j \;\; \psi_j\right]^T_{fuselage}\right) \end{aligned} \tag{18}$$

Now we have the complete boundary conditions for both sides of the wing. The static solution of both sides of the wing gives the force at the root in their local coordinate, $[F1, F2, F3]_{left-wing}$, $[F1, F2, F3]_{right-wing}$. Together with the Euler angles at the root, the force and moment can be transferred into global coordinate.

$$\begin{aligned} \left[F_1 \;\; F_2 \;\; F_3\right]^G_{left-wing} &= T\left(\left[\theta_r \;\; \beta_r \;\; \psi_r\right]^T_{left-wing}\right)^{-1}\left[F_1 \;\; F_2 \;\; F_3\right]_{left-wing} \\ \left[F_1 \;\; F_2 \;\; F_3\right]^G_{right-wing} &= T\left(\left[\theta_r \;\; \beta_r \;\; \psi_r\right]^T_{right-wing}\right)^{-1}\left[F_1 \;\; F_2 \;\; F_3\right]_{right-wing} \end{aligned} \tag{19}$$

And the force applied to the fuselage at the junction in local coordinate will be:

$$\left[F_1 \;\; F_2 \;\; F_3\right]^G_{fuselage} = T\left(\left[\theta_j \;\; \beta_j \;\; \psi_j\right]^T_{fuselage}\right)\left(\left[F_1 \;\; F_2 \;\; F_3\right]^G_{left-wing} + \left[F_1 \;\; F_2 \;\; F_3\right]^G_{right-wing}\right) \tag{20}$$

The moment applied to the fuselage can be calculated in a similar fashion.

In order to take the interactions between adjacent parts into consideration, the calculation of each part needs to be performed in a certain sequence. First, assume some arbitrary values for the loads applied to the fuselage at junction A (the junction between the fuselage and the wing) and at junction B (the junction between the fuselage and the vertical fin), under which the static deformation of the fuselage can be obtained using the beam theory. According to the deformations at junction A and B, the boundary conditions for the wing and the vertical fin can be calculated. The static solution of the wing that satisfies the boundary condition then is calculated. Meanwhile, assume a value for the load that applies at the junction between the fin and the tail, with which the static deflection of the vertical fin that satisfies the boundary condition at junction C (the junction between the fuselage and the fin) can be calculated. Also the deformation of the fin at the junction between the fin and the tail gives the boundary condition of the tail. Then the deformation of the tail can be obtained. After the above procedure is completed, the loads applied to the fuselage and the vertical fin at the three junctions can be updated using present static solutions. Under the new loads, the previous procedures are repeated until the deformation of the whole airplane and the loads at every junction remain unchanged. Then the static solution of the whole airplane is obtained.

3.2 Analysis Results

For demonstration, a simple wing-body-tail beam model and load conditions proposed in [7] are used here. The configuration and properties are shown in Table 1.

Substructure	Length(m)	EA(N)	kGA(N)	EI($N \cdot m^2$)
Fuselage	12	5×10^8	10^8	5×10^6

Wing	30	5×10^8	10^8	10^6
Vertical Fin	3	5×10^8	10^8	5×10^6
Tail	6	5×10^8	10^8	5×10^5

Table 1: Geometry and Property of the Wing-Body-Tail Configuration

The configuration is clamped at the nose and constant normal (initially vertical) follower-forces are applied on the wings and horizontal tails. The wing is flexible and the fuselage will go through a much smaller deformation which is consistent with the configuration of the HALE airplane. Four different load levels are applied and the corresponding deformations are shown in Fig. 6. For each load level, it is found that the whole procedure needs a moderate number of iterations and the time consumed is within a few minutes depending on the load level and number of nodes used.

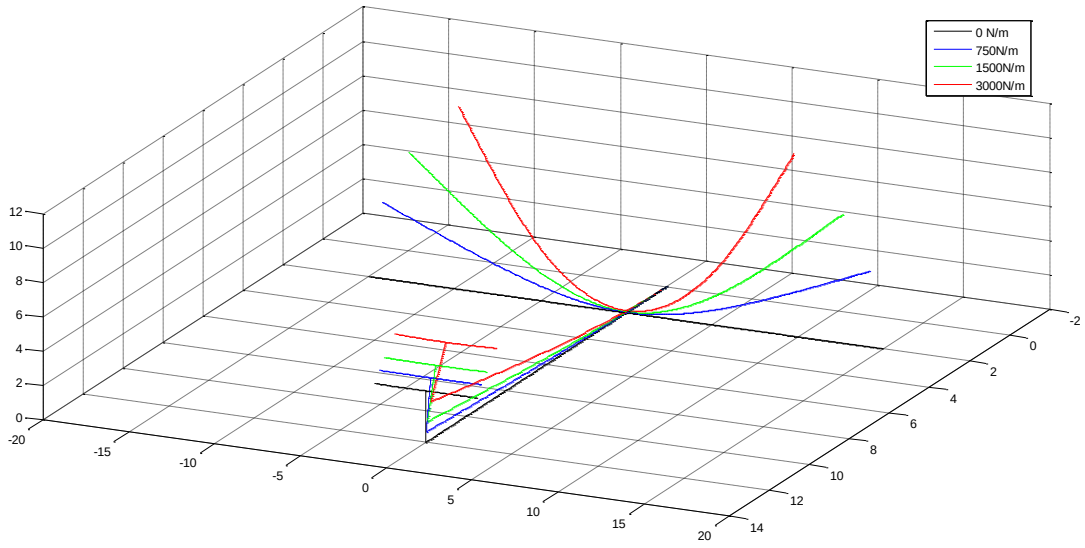

Figure 3: Deformation of wing-body-tail configuration for follower distributed load on wing and tail.

4 AERODYNAMIC MODELING

The aerodynamics will generate forces and moments in the local body frame. In this section, three aerodynamic models are introduced and coupled with the nonlinear beam model. For an accurate representation of the aerodynamics in the presence of three dimensional effects and large beam deformations, a UVLM model is introduced. A vortex lattice model that assumes planar wakes and a simple two dimensional thin-strip model is also used for comparison.

4.1 UVLM Modeling

A vortex element method, based on the unsteady vortex lattice method, has been developed in the present work for investigating the unsteady aerodynamics of a high aspect ratio beam. The developed UVLM algorithm uses three-dimensional velocity smoothing functions to regularize the Biot-Savart law, the free-wake model to simulate wakes dynamics for different wing geometries and dynamics, the vortex shedding model to simulate vorticity shedding

from separating flows at high angle of attack. Verification studies conducted show that the present UVLM is in par with the CFD calculations based on the Euler equations and the Navier-Stokes equations in terms of solution accuracy, but requires only a fraction of computational load. This renders the present UVLM code a suitable design tool for large static deformation studies.

4.1.1 Governing Equations

The unsteady, incompressible flow of Newton fluids is governed by the continuity and momentum equations,

$$\nabla \cdot \mathbf{u} = 0 \tag{21}$$

$$\rho\left(\frac{\partial \mathbf{u}}{\partial t} + (\mathbf{u}\cdot\nabla)\mathbf{u}\right) = -\nabla p + \mu\nabla^2\mathbf{u} \tag{22}$$

where $\mathbf{u}$ is the vector velocity, p and ρ are the fluid pressure and density and μ is its dynamic viscosity. A vortex line is a curve that is tangent to the vorticity vector $\omega \equiv \nabla \times \mathbf{u}$ at each of its points. The circulation (or strength) Γ around a simple closed contour C is defined as the line integral of the velocity along that contour

$$\Gamma = \oint_C \mathbf{u}\cdot dl \tag{23}$$

4.1.2 Biot-Savart Law

The inverse of Eq. (23) is needed to compute the velocity induced by the vorticity. From the continuity equation (21) and the definition of the vorticity (23), it follows that

$$\nabla^2\mathbf{u} = -\nabla\times\omega \tag{24}$$

Then, the velocity $\mathbf{u}$ at a point x may be recovered using an integral over the volume V where vorticity $\omega(\mathbf{x}')$ is non-zero (see for example Saffman [8] for details) and can be reduced to a surface integral $(\omega \mathrm{d}V = \gamma \mathrm{d}S)$,

$$\mathbf{u}(x) = \frac{1}{4\pi}\int_V \frac{\mathbf{x}-\mathbf{x}'}{|\mathbf{x}-\mathbf{x}'|^3}\times\omega(\mathbf{x}')dV = \frac{1}{4\pi}\int_S \frac{\mathbf{x}-\mathbf{x}'}{|\mathbf{x}-\mathbf{x}'|^3}\times\gamma(\mathbf{x}')dS \tag{25}$$

which is known as the Biot-Savart law. In the presence of solid boundaries, an extra term $(\nabla\phi)$ must be added to the right-hand side of (25) associated with the homogeneous solution of (24). Typically, this contribution is computed with a boundary element method. The vortex panel method discussed later is applied in this work.

Vortex filaments are space curves with finite circulation and a zero cross sectional area. For these cases $(d\Omega = ds\mathbf{n}\cdot d\mathrm{x}')$, the circulation can be taken out of the integral,

$$\mathbf{u}(\mathbf{x}) = \Gamma\int_{C(u)} \mathbf{K}(\mathbf{x}-\mathbf{x}(u))\times\frac{\partial\mathbf{x}(u)}{\partial u}du \tag{26}$$

where a vortex filament is represented with a time-dependent, parametric space curve $C(u)$, x(u) is the position vector of a point u on $C(u)$, $\mathbf{K}(\mathbf{r}) = \left(\frac{1}{4\pi}|\boldsymbol{r}|^3\right)\mathbf{r}$ is the Biot-Savart kernel, $\mathbf{r} = \mathbf{x} - \mathbf{x}(u)$ and **x** is the position vector of a point where the velocity **u** is evaluated.

4.1.3 Velocity Smoothing Functions

The integrand in Eq. (25) is singular as $\mathbf{r} \to 0$. This results in unphysically high induced velocity at a point very near to a vortex filament. A smoothing method is used to regularize the Biot-Savart law so as to remove the singular part from computations.

In the smoothing method, the singular Biot-Savart kernel $\mathbf{K}(\mathbf{r})$ is replaced with a mollified kernel $\mathbf{K}_{\boldsymbol{\sigma}}(\mathbf{r})$ which removes the singular behavior at the vortex center line,

$$\mathbf{K}_\sigma(\mathbf{r}) = -\frac{g_\sigma(\mathbf{r})}{|\mathbf{r}|^3}\mathbf{r} \tag{27}$$

where $\mathrm{g}_{\boldsymbol{\sigma}}(\mathbf{r}) = \mathrm{g}_{\mathbf{3}}(\rho)$ is a three-dimensional velocity smoothing function [9] with σ the core size and ρ the relative distance of a point with respect to a point on a filament,

The regularized Biot-Savart law can now be written as

$$\mathbf{u}(\mathbf{x}) = \Gamma\int_{C(u)} \mathbf{K}_\sigma(\mathbf{x} - \mathbf{x}(u)) \times \frac{\partial \mathbf{x}(u)}{\partial u} du = -\Gamma\int_{C(u)} \frac{g_3(\rho)}{|\mathbf{r}|^3}\mathbf{r}\frac{\partial \mathbf{x}(u)}{\partial u} du \tag{28}$$

Given a three-dimensional vorticity smoothing function $\zeta_3(\rho)$, the associated three-dimensional velocity smoothing function $\mathrm{g}_{\mathbf{3}}(\rho)$ can be found from [9]

$$g_3(\rho) = \int_0^\rho \zeta_3(t) t^2 dt \tag{29}$$

4.1.4 Vortex Panel Method and Aerodynamic Forces

The vortex panel method is based on linear potential flow, which reduces the continuity equation to Laplace's equation,

$$\nabla^2\phi = 0 \tag{30}$$

Using the Green's theorem, a solution can be obtained by distributing elementary solutions on the problem boundaries (which may include wakes shed from solid boundaries). Solid geometry is represented using a finite set of quadrilateral panels with constant distribution of circulation strength Γ_i per panel.

Under the assumption that the wake panel's strength Γ_ω remains unchanged at the value when it is shed, a system of linear equations can thus be formed,

$$\mathbf{A\Gamma = b} \tag{31}$$

where a_{ij} is the unit influence of panel *j* at the collocation point of panel *i*.

Solution of Eq. (31) will provide the velocity potential and the velocity components. Once the flowfield is determined the resulting pressures can be computed by the Bernoulli equations [10]. The pressure coefficient can be computed for each panel as

$$C_p = \frac{p - p_{ref}}{\frac{1}{2}\rho u_{ref}^2} = \frac{(\nabla\phi)^2}{u_{ref}^2} + \frac{2}{u_{ref}^2}\left[\mathbf{u}_0 + \Omega \times \mathbf{r}\right]\cdot\nabla\phi - \frac{2}{u_{ref}^2}\frac{\partial\phi}{\partial t} \tag{32}$$

where $-[\mathbf{u}_o + \Omega \times \mathbf{r}]$ is the kinematic velocity of the undisturbed fluid due to the motion of the wing as viewed in the body frame of reference.

The total pressure force is obtained by integrating the pressure difference over all panels:

$$\mathbf{f} = \sum_{k=1}^{N}\int_{S_k}\Delta p\mathbf{n}\mathrm{d}S = \sum_{k=1}^{N}\int_{S_k}\rho\left[\left(\frac{u_t^2}{2}\right)_u - \left(\frac{u_t^2}{2}\right)_l + \left(\frac{\partial\phi}{\partial t}\right)_u - \left(\frac{\partial\phi}{\partial t}\right)_l\right]\mathbf{n}\mathrm{d}S \tag{33}$$

4.1.5 Wake Modeling Methods

Wake modeling concerns the transport of vorticity in the wake, the mechanism by which such vorticity is shed from solid boundaries, and its interactions with solid boundaries. Various wake modeling methods have been devised. Because the wake is vortical in nature, either fulamentary or sheety in spatial characteristics, vortex method is the method of choice to model its dynamics. Vortex filaments and vortex sheets are often used to represent the wake mathematically. A method that approximates the vortex sheets using simple elements is use dto compute velocity induced by vortex sheets. The relaxation free wake model [11] which uses an iterative or relaxation solution method is in use to find the force-free shape of the wake.

4.2 Vortex Lattice Modeling

The second model is a linear unsteady vortex lattice aerodynamic model in discrete time domain. For the static calculation investigated here, the time derivatives are skipped to calculate the steady-state result efficiently. Mode shapes and slope of mode shapes are utilized to calculate the aerodynamic forces of the entire wing. In this vortex lattice model, all the vortex sheets are assumed planar, which is correct only when the deflection is small.

4.3 Simple Aerodynamics

The third aerodynamic model is a simple two dimensional one based on incompressible, inviscid flow. Drag and side force are ignored. The lift and moment are calculated based on local angle of attack. The 2D airfoil lift curve slope 2π is used and the lift is calculated at the aerodynamic center. The moment is calculated around the elastic axis of the airfoil, which will be used as the reference line of the beam model.

4.4 Coupling with Beam Model

Combination of all the afore-mentioned structural and aerodynamic modeling techniques provides a full description of the large static deformation of flexible beam in a free airflow. Our main concern is in the evaluation of all the aerodynamic loads in situations with large

beam deflections and effect of elastic deformations on the aerodynamic lift and moment distribution.

Coupling with the CFD model is quite straightforward. With an initial angle of attack and the undeformed shape of the beam, the CFD model produces loads at every FEM grid point. The beam model is defined based on the FEM model. One corresponding node is generated on the reference line to each FEM grid point on the beam. Then the aerodynamic forces and moments are transferred to the reference line and the loads applied to the reference line only are obtained. Since the force offered by the CFD model is a point load, to obtain the equivalent distributed loads, every element along the reference line is divided into two identical elements and each load is distributed around that node, i.e., on the two adjacent elements (only one adjacent element for node at the tip and root). The static deformation of the reference line is calculated under this load and the deformations of those corresponding nodes are picked out. With the assumption that the cross-section behaves rigidly, the displacement of ith FEM grid point $[u\ v\ w]^T_{FEM-i}$ can be expressed as:

$$\begin{aligned} T^i_{ini} &= T\left[\theta\ \ \beta\ \ \psi\right]^T_{initial-i} \\ T^i_{pre} &= T\left[\theta\ \ \beta\ \ \psi\right]^T_{present-i} \end{aligned} \tag{34}$$

$$\left[u\ v\ w\right]^T_{FEM-i} = \left[x\ y\ z\right]^T_{beam-i} + T^i_{pre}T^i_{ini}\left(\left[x_0\ y_0\ z_0\right]^T_{FEM-i} - \left[x_0\ y_0\ z_0\right]^T_{beam-i}\right) - \left[x_0\ y_0\ z_0\right]^T_{FEM-i} \tag{35}$$

where $[\theta\ \beta\ \psi]^T_{initial-i}$ and $[\theta\ \beta\ \psi]^T_{present-i}$ represent the Euler angles at the corresponding node of ith FEM grid point before and after deformation respectively. $[x_0\ y_0\ z_0]^T_{beam-i}$ and $[x\ y\ z]^T_{beam-i}$ are the coordinates at the corresponding node of ith FEM grid point before and after deforming respectively. $[x_0\ y_0\ z_0]^T_{FEM-i}$ is the coordinates of the FEM node before deformation. Then the displacements used in the CFD part are updated and the new forces and moments on each grid point are calculated. The prescribed procedure is repeated till the displacements or the forces don't change anymore.

Since the Vortex Lattice model calculates the lift and moment of the whole beam, a method similar to calculating the stiffness matrix is implemented here to calculate the aerodynamic forces on each element. In the Vortex Lattice model, the beam is divided into a finite number of panels spanwise and chordwise. Those panels along the same chord are regarded as one element and lift and moment are calculated on each element. Two kinds of mode shapes are utilized: a unit transformation of one single element and a unit rotation of one single element. Together with an initial angle of attack, the transformation mode shape gives the lift on that transferred element and the rotation mode shape gives the moment on that rotated element. The loads applied on the beam model can be obtained by adding up those forces and moments together. Like the CFD model, the loads are point loads and the number of nodes is doubled due to the need of distributing the loads. Then the static deformation and the angle of attack of each element are calculated using the beam theory. With the updated angle of attack, the new lift and moment are obtained. The above procedure is repeated till the deformations and the loads no longer change.

For large deformations, the relationship between Euler angles and local angle of attack is developed here. For a general aircraft orientation, the angle of attack alpha and sideslip gamma are defined in Figure 4:

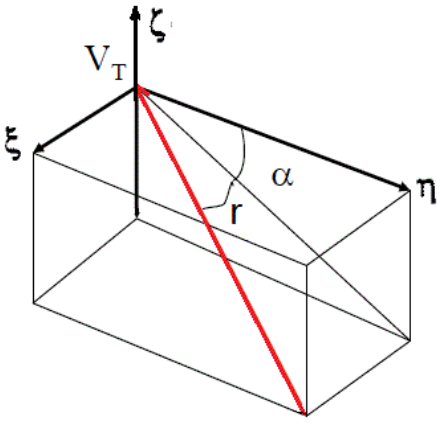

Figure 4: Definition of angle of attack α and side slip γ

The inflow can be described in the local coordinate as follows:

$$\left(\vec{V}_T\right)_L = \left[-sin\gamma \; -cos\gamma cos\alpha \; cos\gamma sin\alpha\right]^T \tag{36}$$

For an initial angle of attack α_0 and sideslip γ_0, the inflow can be described in the global coordinate as follows:

$$\left(\vec{V}_T\right)_G = \left[-sin\gamma_0 \; -cos\gamma_0 cos\alpha_0 \; cos\gamma_0 sin\alpha_0\right]^T \xrightarrow{\gamma_0=0} \left[0 \; -cos\alpha_0 \; sin\alpha_0\right]^T \tag{37}$$

The local inflow rotates to the global coordinate via the transformation matrix:

$$\left(\vec{V}_T\right)_L = T \cdot \left(\vec{V}_T\right)_G \tag{38}$$

The local angle of attack can be obtained from the above equation:

$$\alpha = -arctan\left(\frac{sin\gamma T(3,3) - cos\gamma T(3,2)}{sin\gamma T(2,3) - cos\gamma T(2,2)}\right) \tag{39}$$

The coupling procedure with the simple aerodynamics model is similar to coupling with the Vortex Lattice model. The beam is also divided into a number of elements. With an initial angle of attack or a built-in angle at the beam root, the lift and moment around the reference line on each element can be calculated. Under this load, the beam model is used to calculate the deformation of the reference line, based on whose result the new local angle of attack can be obtained and is passed back to calculate the aerodynamics on each element. This procedure is repeated until the deformation of the beam or the aerodynamics loads become steady.

4.5 Analysis Results of Large Deflection under Different Aerodynamics

The flat beam specimen with $[0/90]_{3s}$ lay-up with no elastic couplings proposed in [1] is used with the three different aerodynamic models. The beam is 0.56m long in span direction and 0.03m chordwise. The beam is $1.49 \times 10^{-3} m$ thick and the density is $1530\, kg/m^3$. The stress-strain is diagonal since there this no coupling. And $E_{11} = 3.7 \times 10^6 N$, $E_{22} = 8.7 \times 10^6 N$, $E_{33} = 2.9 \times 10^5 N$, $E_{11} = 0.183 N \cdot m^2$, $E_{11} = 0.707 N \cdot m^2$, $E_{11} = 276 N \cdot m^2$.

For comparison, an initial angle of attack of 5 degree is used to generate large deformation. The comparison of the static deformations, including the Euler angles and displacements of the reference line, and the aerodynamic force and moment applied on the reference line in the global coordinates at speed equal to 20m/s and 23m/s are shown in Figure 5-12.

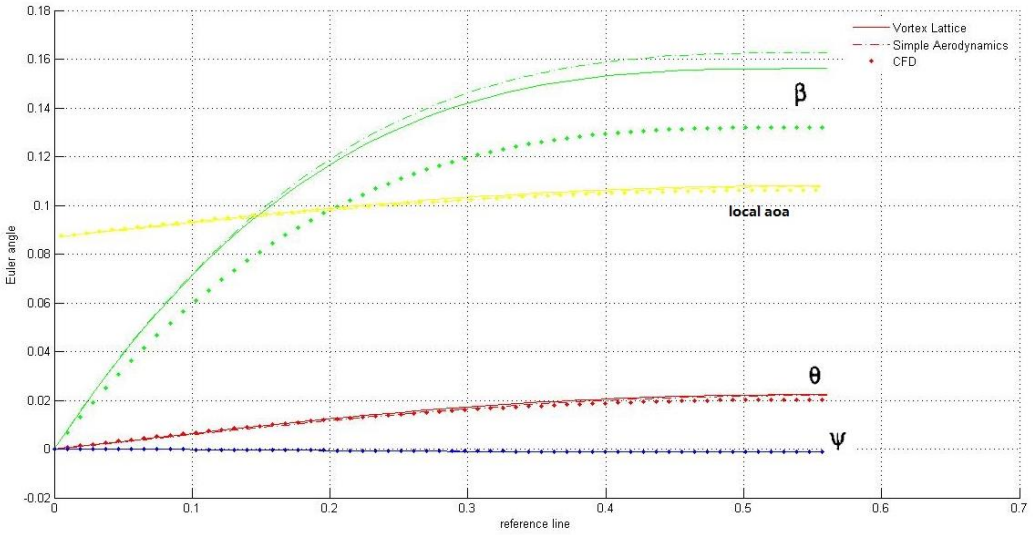

Figure 5: Euler angles of the reference line at speed 20m/s

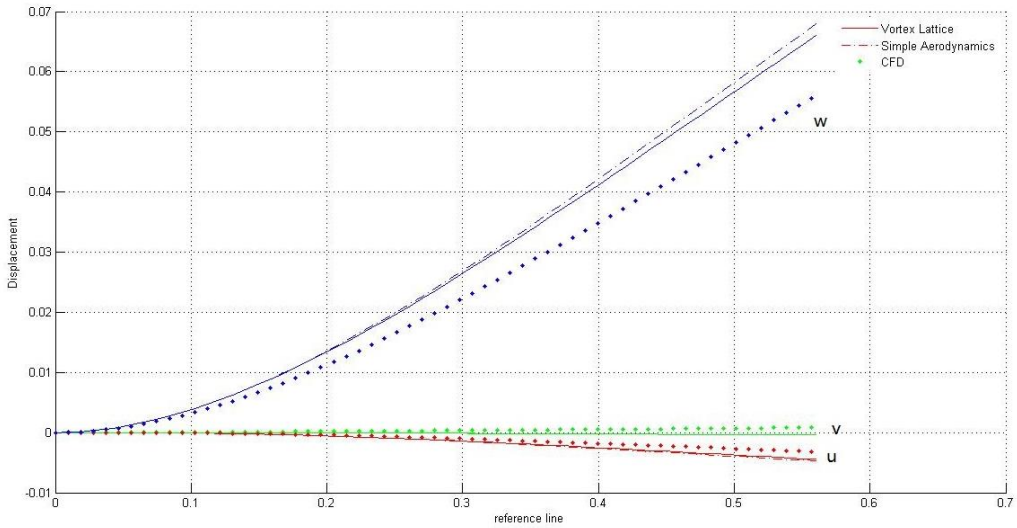

Figure 6: Displacement of the reference line at speed 20m/s

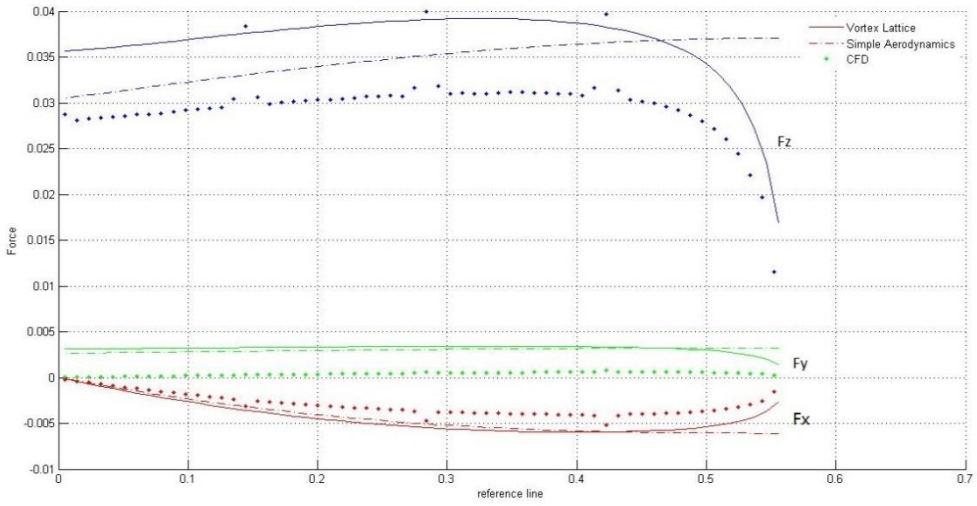

Figure 7: Force in global coordinate applied on the reference line at speed 20m/s

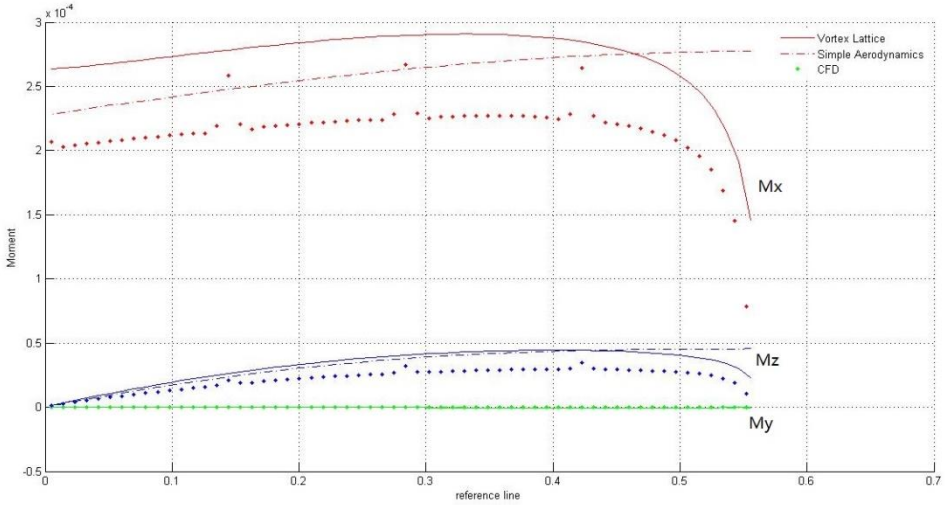

Figure 8: Moment in global coordinate applied on the reference line at speed 20m/s

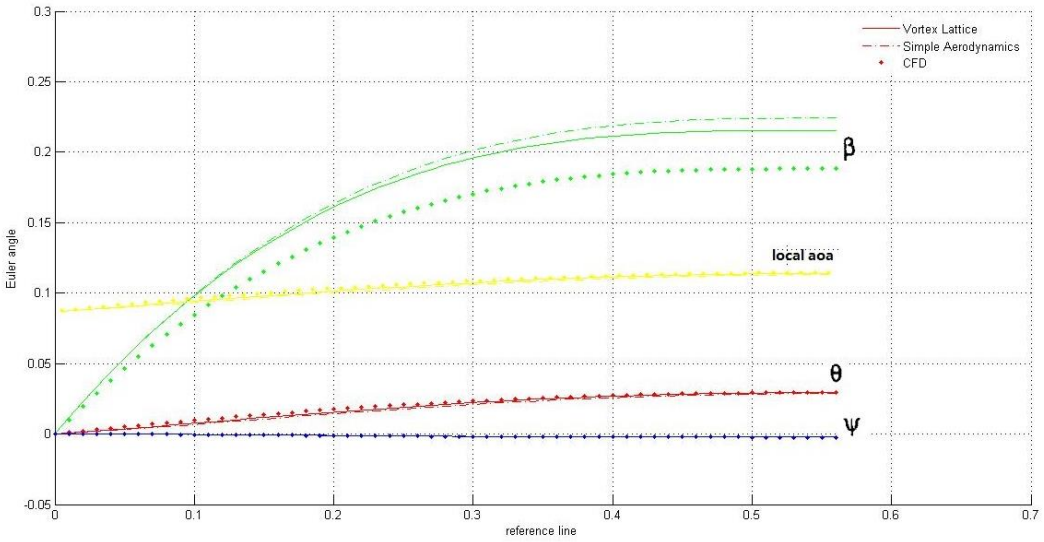

Figure 9: Euler angles of the reference line at speed 23m/s

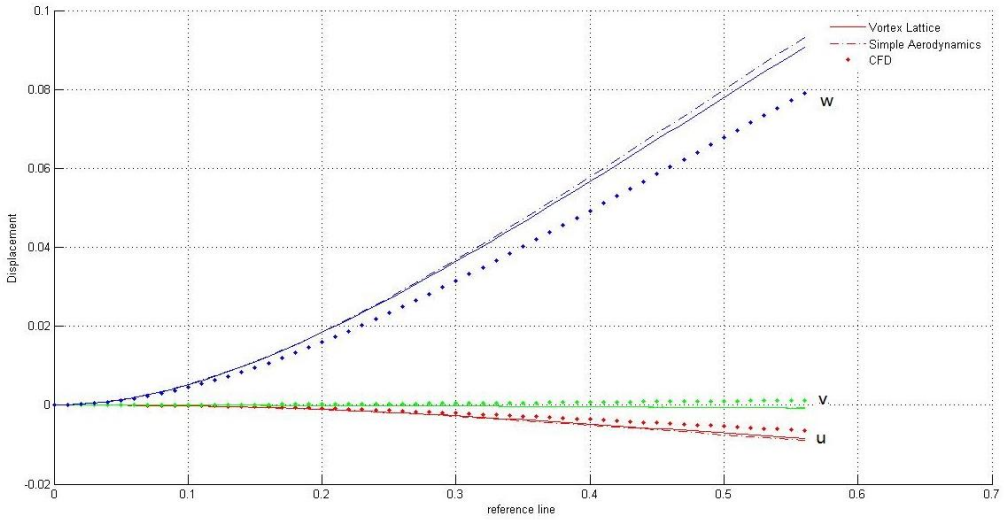

Figure 10: Displacement of the reference line at speed 23m/s

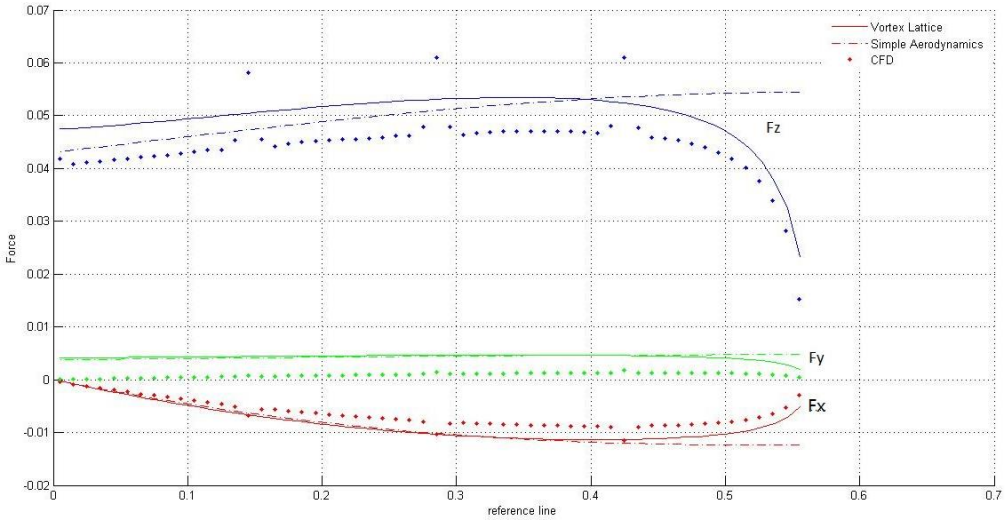

Figure 11: Force in global coordinate applied on the reference line at speed 23m/s

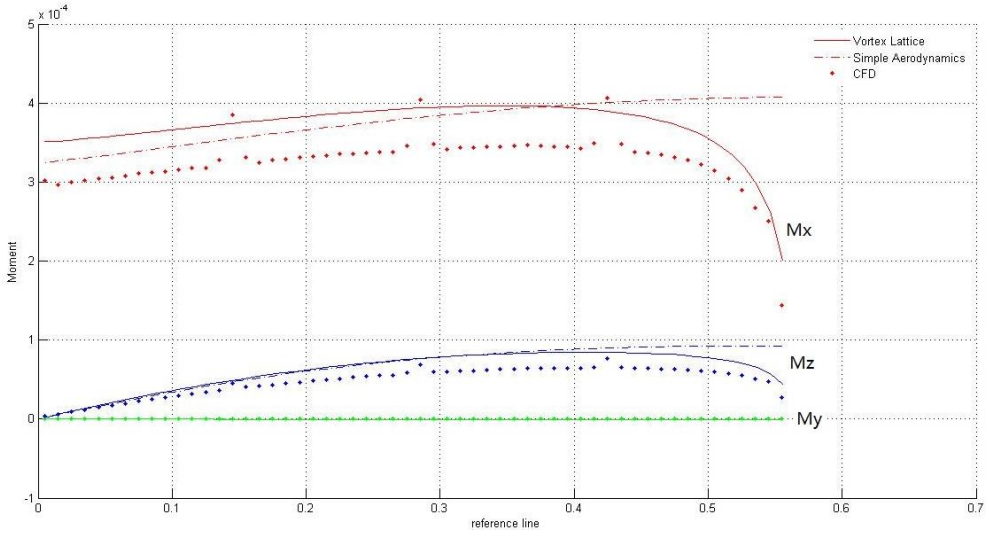

Figure 12: Force in global coordinate applied on the reference line at speed 23m/s

As can be seen from the figures, the results of the three models match well. The CFD model produces a slightly smaller deformation due to the 3D effect, vortex sheets roll-up reducing the lift. These 3D effects will increase as the deformation increases.

Figure 13 shows the developing history of half span using the CFD model at speed 20m/s. It took only 6 iterations for the model to converge to the static position.

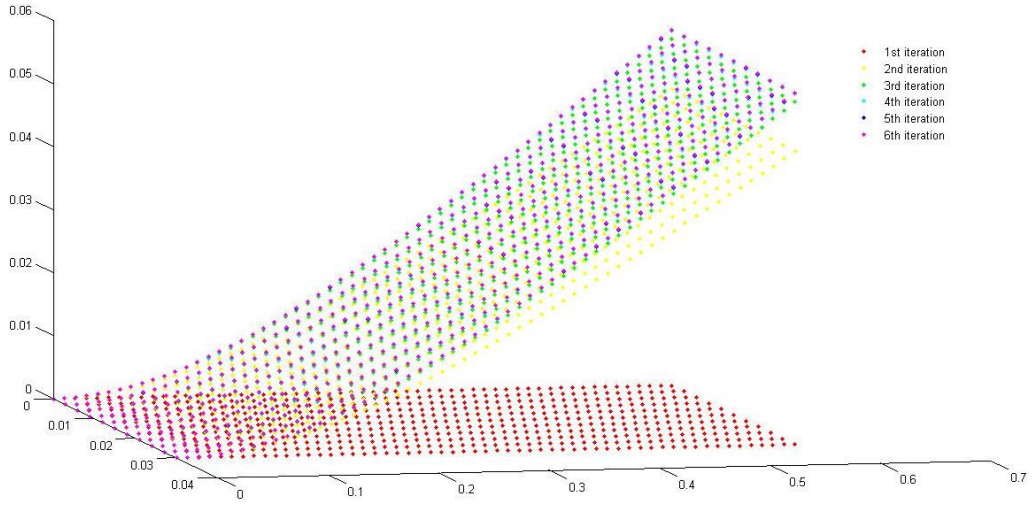

Figure 13: Developing history of half span at 20m/s

The flutter speed can be roughly estimated based on the natural frequencies vs. tip deflection plots in Minguet's and Dugundji's work which is shown in Figure 14. For all the three different aerodynamics employed, the tip deflection is about 11% of the beam length at speed 20m/s. From Figure 14, it can be seen that the torsional natural frequency decreases from 85Hz to 42Hz for this amount of the tip deflection. Based on a simple 2D approximation, the flutter speed is proportional to the torsional frequency. Thus, the flutter speed is found to be about 54m/s at this tip deflection. Since the tip deflection goes up as the flow speed increases. Using the same method, the flutter speed of this beam is estimated to be around 27 m/s with tip deflection at that speed.

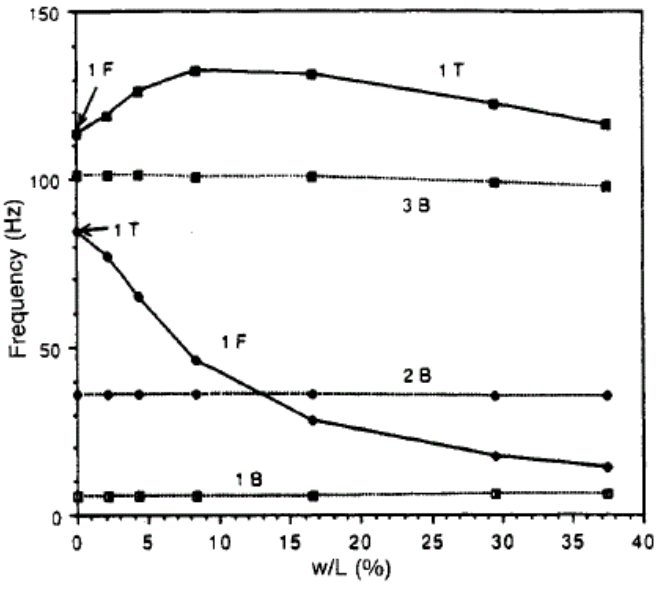

Figure 14: Changes in natural frequencies for $[0/90]_{3s}$ beam with increasing tip deflection

As for static divergence, for an idealized rectangular cantilever wing it can be estimated using the following equation[13]:

$$U_{div} = \frac{\pi}{cs}\sqrt{\frac{GJ}{2\rho ae}} \tag{40}$$

where c is the chord length, GJ is the torsion stiffness, a is the lift-curve slope and e is the ratio expressing the eccentricity of the aerodynamic center. For the beam under study here, the static divergence speed is about 45m/s when using 2π as the lift-curve. Based on the estimation of static divergence speed and flutter speed we decided not to increase the air speed beyond 23m/s.

5 CONCLUSION

In this present paper a methodology has been developed for dealing with the nonlinear large deformation of HALE plane using a set of twelve nonlinear differential equations based on the use of Euler angles and transformation matrix together with Newton-Raphson iteration technique. This structural model is an important step towards building numerically-efficient methodology to investigate the aeroelastic behavior of the HALE airplane.
The studies employing the three different aerodynamic modeling methods have looked into the importance of three-dimensional effects on wings with large deflections. The mutual effects between elastic deformation and lift distribution are analyzed by coupling the structural model and the aerodynamic model. The outcomes of the present study provide good guidelines for flutter analysis in the future.

Acknowledgement

The first author kindly acknowledges the NUS PhD Scholarship program which has been providing the financial support throughout the research period.

6 REFERENCES

[1] Minguet P, Dugundji J. Experiments and analysis for composite blades under large deflections. I-Static behavior, [J]. *AIAA journal*, 1990, 28(9): 1573-1579.

[2] Minguet P J. Static and dynamic behavior of composite helicopter rotor blades under large deflections [D]. Massachusetts Institute of Technology, 1989.

[3] Kim T. Nonlinear large amplitude structural and aeroelastic behavior of composite rotor blades at large static deflection [D]. Massachusetts Institute of Technology, 1992.

[4] Roccia B A, Preidikman S, Massa J C, et al. Modified unsteady vortex-lattice method to study flapping wings in hover flight [J]. *AIAA journal*, 2013, 51(11): 2628-2642.

[5] Katz J, Plotkin A. Low-speed aerodynamics [M]. Cambridge University Press, 2001.

[6] Pai P F. Highly flexible structures: modeling, computation, and experimentation[M]. AIAA (American Institute of Aeronautics & Ast, 2007.

[7] Palacios R, Murua J, Cook R. Structural and aerodynamic models in nonlinear flight dynamics of very flexible aircraft[J]. AIAA journal, 2010, 48(11): 2648-2659.

[8] Saffman P G. Vortex dynamics[M]. Cambridge university press, 1992.

[9] Winckelmans G S, Leonard A. Contributions to vortex particle methods for the computation of three-dimensional incompressible unsteady flows[J]. Journal of Computational Physics, 1993, 109(2): 247-273.

[10] Katz J, Plotkin A. Low-speed aerodynamics[M]. Cambridge University Press, 2001.

[11] Leishman J G, Bhagwat M J, Bagai A. Free-vortex filament methods for the analysis of helicopter rotor wakes[J]. Journal of aircraft, 2002, 39(5): 759-775.

[12] Minguet P, Dugundji J. Experiments and analysis for composite blades under large deflections. II-Dynamic behavior[J]. AIAA journal, 1990, 28(9): 1580-1588.

[13] Fung Y. An introduction to the theory of aeroelasticity[M]. Courier Corporation, 2002. pp.85-90

7 COPYRIGHT STATEMENT